AIAA SciTech Forum
23-27 January 2023, National Harbor, MD & Online
AIAA SCITECH 2023 Forum

10.2514/6.2023-1408

Angular Properties of Ionic Liquid Electrospray Emitters

Madeleine R. Schroeder*, Ximo Gallud†, and Amelia R. Bruno‡
Massachusetts Institute of Technology, Cambridge, USA

Oliver Jia-Richards§
University of Michigan, Ann Arbor, USA

Paulo C. Lozano¶
Massachusetts Institute of Technology, Cambridge, USA

The angular distribution of emitted species in electrospray ion beams is not well characterized and can have negative effects on propulsive performance and emitter lifetime. We present an experimental characterization of the angular distribution of emitted species in a single electrospray ion beam as a function of firing voltage using time of flight mass spectrometry. Angular current distributions indicate the central axis of emission varies up to 10° from the central axis of the emitter tip. Variation in the ion species as a function of angle depends on the firing voltage. Simulations of single particle trajectories indicate that fragmentation of ion clusters results in ion products moving closer to the center of the beam and neutral products spreading up to 47° depending on how rapid fragmentation occurs. Experimental results are compared to multiscale full-beam simulations of electrospray emission and future use of these simulations to explain angular beam behavior is discussed.

I. Introduction

Electrospray emission evaporates ions and solvated ion clusters from the surface of an ionic liquid using an electric field created by applying voltage between the ionic liquid and an extractor with an aperture. The acceleration of these clusters in the electric field produces thrust that is useful for maneuvering small satellites in low Earth orbit and attitude control for larger satellites. An important aspect of designing electrospray emitters is understanding the emission characteristics of different ion species. Emission of a wide mass distribution of species will negatively impact performance, reducing propulsive efficiency and increasing focused ion beam spot size [1–3]. Fragmentation of larger ion clusters after emission is often observed in pure ion mode electrospray thrusters and is known to further reduce propulsive efficiency [1, 2]. Additionally, the low energy ions and neutral clusters resulting from fragmentation events can leave ionic liquid deposits on the extractor, degrading the hardware and leading to electrical shorts that dramatically reduce emitter lifetime [4, 5].

Previous work by Coles [1, 6] and Miller [7] has investigated the impact of firing voltage, ionic liquid selection, and liquid temperature on the ion beam mass composition and quantified its impacts on propulsive efficiency. Experiments and molecular dynamics simulations have been performed to characterize fragmentation rates of different emitted species as a function of ionic liquid, cluster internal energy, and applied electric field [7–9]. N-body simulations that propagate the full ion beam of a single emitter through a realistic electric and potential field have been used to simulate ion beam diagnostics including retarding potential analysis (RPA) curves [10, 11], which provide insight on fragmentation events in the sampled beam; most published results sample the beam centerline [12, 13].

Limited experiments have been performed to characterize the angular distribution of species. Some experiments with single emitters have shown that the center of the beam contains a higher percentage of single ions while the outer edges of the beam contain a higher percentage of larger clusters and sometimes even droplets [14]. Other experiments with full arrays of emitters have not been able to resolve any trends in angular beam composition [15]. However, little work has been done to characterize the dependence of this angular species distribution on emission parameters such as firing voltage. Moreover, the underlying cause of angular-dependent species distribution is not well understood. In

*Doctoral Candidate, Department of Aeronautics and Astronautics, Student Member AIAA.
†Doctoral Candidate, Department of Aeronautics and Astronautics, Student Member AIAA.
‡Doctoral Candidate, Department of Aeronautics and Astronautics, Student Member AIAA.
§Assistant Professor, Department of Aerospace Engineering, Member AIAA.
¶Miguel Alemán-Velasco Professor, Department of Aeronautics and Astronautics, Associate Fellow AIAA.

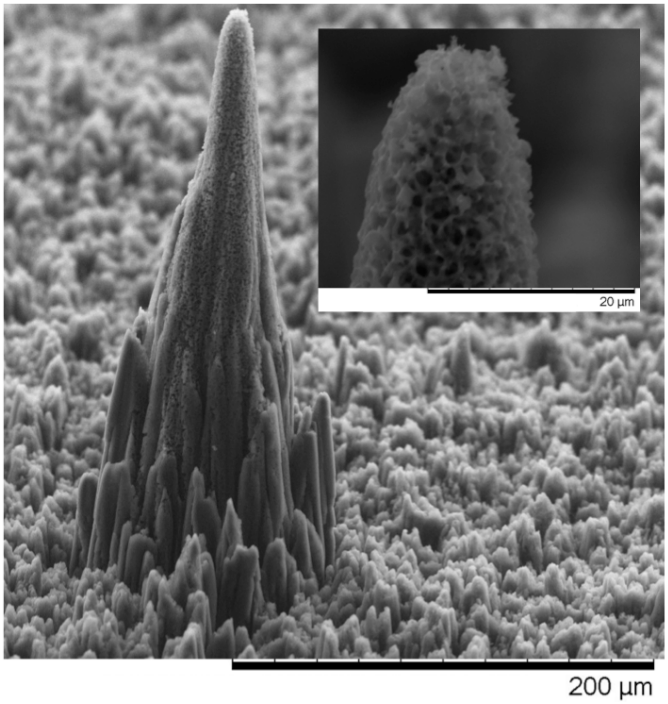

Fig. 1 Scanning electron microscope image of the porous carbon emitter used in these experiments.

particular, spatial dependence of species emission on the meniscus and the effect of fragmentation on angular beam composition are unclear. Characterizing these effects is key to accurately quantifying the efficiency of electrospray emitters and developing methods of reducing unwanted beam spreading.

To address this gap in understanding of electrospray emission, we present an experimental characterization of species angular distribution for a single emitter using the liquid EMI-BF_4 with different applied voltages. Using the same simulation framework as recent N-body simulations [5, 11], we investigate trajectories of single clusters in realistic emitter electric and potential fields to determine the effect of fragmentation on cluster trajectories. We also present preliminary results of N-body simulations of angular beam composition for comparison to experimental results, and discuss how these simulations could be used in future work to reduce uncertainty in knowledge of the initial conditions of ion clusters after emission.

II. Methodology

A. Ion Source

All experiments were performed with a single porous carbon emitter [16]. Figure 1 shows a scanning electron microscope image of the porous carbon tip used in these experiments. The single carbon emitter was centered in a square centimeter of porous carbon substrate. An extractor grid with a 300 µm diameter aperture was placed with the apex of the tip in plane with the bottom of the extractor grid. The tip was loaded with EMI-BF_4 that had been dried for 24 hours at <1e-3 Torr. The propellant was applied to the back of the carbon substrate, where it would then passively flow through the carbon bulk and into the tip. The tip was then mounted onto a rotational stage and the full assembly was placed under vacuum for 24 hours before testing began. High positive and negative voltage was applied to the liquid in the porous carbon via a spring acting as a distal electrode at the back of the carbon substrate. The extractor was kept grounded throughout all tests. The tip was conditioned by firing with a 900 V square wave with period 10 seconds for 10 minutes before data was collected.

B. Time of Flight Mass Spectrometry

Time of flight mass spectrometry (TOF) was used to analyze the portion of the beam composed of each ion cluster species. TOF measurements were taken by firing the ion source at a Channeltron Electron Multiplier (CEM). An electrostatic deflection gate between the source and the detector is periodically pulsed to interrupt the flow of the ion beam to the CEM. The time it takes for ion clusters to travel from the gate to the CEM, t_{TOF}, depends on their charge-to-mass ratio and the potential over which the cluster was accelerated. Equation 1 gives the flight time for an unfragmented ion or cluster with mass m, charge q, and firing voltage V_0.

$$t_{TOF} = \frac{L_{TOF}}{\sqrt{2\frac{q}{m}V_0}} \tag{1}$$

Ion clusters that fragment in the electric field region between the emitter tip and the extractor plate have flight times between those of unfragmented clusters and the charged product of the fragmentation. L_{TOF} is the distance that the ions must travel between the electrostatic gate and the CEM, which is 1.12 m in the experimental setup used in this work. The current detected by the CEM was amplified by a factor of $\sim 10^5$ by the CEM and ~50 by an op-amp circuit with a rise time of less than 30 ns and monitored with a Keysight DOSX3024A oscilloscope. The gate was operated with an Agilent 33220A signal generator and a DEI PVM-2410 pulse amplifier set to ±950 V. The gate was pulsed at 300 Hz. The signal at the oscilloscope was averaged over 10 seconds of firing, yielding 3,000 averages.

Different locations in the beam were sampled by rotating the source to the desired angle and sampling the beam. The zero angle is defined when the central axis of the emitter tip is perpendicular to the electrostatic gate used for beam deflection. The area of the detector was approximately 5×10^{-5} m^2. At a distance of 1.12 m from the ion source, this was considered to be a point detector.

C. Current Characteristics

Current vs. voltage curves were taken for varying firing voltages after conditioning was completed. These curves were obtained by averaging current measurements taken from the high voltage power source used to fire the emitter. Intercepted current was measured from the extractor grid. Firing voltage was increased linearly from 0 to 950 V over 60 seconds. This was repeated 6 times and the results were averaged. Linear fits were applied to different regions of the curve to determine the rate of current increase with voltage increase.

Angular current measurements were taken using the TOF detector. The amplification of the CEM was kept constant during the tests so the magnitude of the signal at the CEM indicates the relative magnitude of the beam signal reaching the detector, and thus the relative magnitude of the beam signal at each part of the beam. This allows for comparison between the signal magnitudes at varying voltages and locations in each of the beams characterized. Current measurements were taken at approximately single degree increments from the left edge of the beam to the right edge of the beam. The edges are defined as the angles at which the detector signal was indistinguishable from background noise. Third-order polynomials were then fit to the angular current data points to demonstrate possible beam current distributions.

D. Experimental Data Processing

The reltive beam composition for different species was obtained from the TOF curves using an ensemble Kalman filter based post processing technique [17].

Full beam time of flight measurements are difficult to collect, as spreading effects from the angular distribution of the beam would necessitate either picosecond rise times in the amplifying electronics or a full-beam current collector larger than most standard vacuum chambers. Direct full beam time of flight measurements are not possible with this setup. However, angular time of flight measurements combined with angular current density measurements can be used to estimate the full beam composition. For this work we assumed the beam mass composition and emitted current are axisymmetric. The emitted current density angular distribution, $I(r)$, is then a function only of r, the distance from the center of the beam. $I(r)$ is divided into sections at the angles halfway between those of each measured time of flight curve. These sections likely contain a similar beam composition to that found in each one of the measured time of flight curves. The calculated full beam time of flight curve is found by adding the individual time of flight curves weighted by the percentage of the beam that is in the section containing that time of flight curve. The weights are found by integrating I(r) over each section of the beam in spherical coordinates.

E. N-body Full Beam Simulation

The N-body simulation results presented in this work were generated using the same procedure as developed in Petro et al. [5, 10, 11]. Particles are injected into the simulation according to initial conditions of emission current density as given by electrohydrodynamic (EHD) solutions for meniscus shapes from models developed by Coffman [18] and Gallud-Cidoncha [19, 20]. The EHD simulations described in these references were repeated for emitter geometries matching the experimental geometry of the emitter used in this work. The tip profile was taken from the SEM image in Figure 1 using edge-detecting techniques. An axially symmetric average profile of the tip contour was extracted and meshed during preprocessing for the electrohydrodynamic model. Forces between ions are resolved each timestep to propagate ions and ion clusters through the electric field. The ion-ion component of the electric field (Poisson) is computed using the Barnes-and-Hut approximation of Coulombic interactions [21] to reduce the computational effort [22]. This contribution of the electric field is added to the background field created by the extractor-tip geometry (Laplace). The Laplace component is interpolated from the EHD model. Fragmentation is included at each timestep according to the mean lifetimes of different cluster types as determined in previous work with simulated RPA curves and molecular dynamics results [9, 11]. Single particles trajectories are found using the same simulation procedure without including the Poisson field created by other ions in the beam. For such low currents (below 120 nA), it can be shown that the Poisson contribution of the field is negligible [11].

Angular beam current distribution is calculated using the same post processing used in Petro et al., which finds the number of particles in the simulation crossing a spherical boundary per unit time and area [11]. Angular beam composition is calculated in the same way but the current density is divided into the different cluster species that are plotted as current fraction as a function of angle.

III. Results and Discussion

A. Experimental Emitter Behavior

1. Current

Figure 2 shows the current vs. voltage curve for the single carbon emitter. Emission becomes detectable at a startup voltage of 800 V. Between 810 V and 950 V current increases linearly to 50 nA at a slope of 0.32 nA/V. The intercepted current remains below 2 nA, which is within noise level of the current amplification electronics. At 950 V the slope of the IV curve increases by a factor of 16 to 5.28 nA/V and the intercepted current increases to 25 nA, indicating at least secondary meniscus formation. Increases in intercepted current at these voltages suggests at least one of the multiple emission sites is more significantly off axis than the primary site observed between 800 V and 950 V.

Figure 3 shows the angular current distributions for four representative voltages between 800 V and 950 V. These current profiles were determined from the magnitude of the time of flight signal detected at the CEM. The angular current distribution curves were normalized by the maximum detected signal for each voltage for easier comparison between the distributions. The minimum detectable signal relative to the maximum signal decreases as the voltage increases due to the increase in emitted current. Table 1 gives the angles for the center, total spread, full width at half maximum (FWHM), of the beam and the total signal magnitude detected by the CEM. For the lower voltages the actual beam spreading angle will be slightly larger than the values presented here as the edges of the beam were more difficult to measure at the lower current levels. At 800 V the meniscus is nearly centered on the tip. As the voltage increases the meniscus shifts first to the right then to the left. At 950 V we observe multiple emission sites. One is located just left of the meniscus observed at 900 V while the other is approximately 30 degrees to the right of the primary meniscus. The relative magnitude of the two menisci for this case suggests that the right meniscus is off axis in the direction orthogonal to that investigated in these angular scans.

2. Beam Composition

Figures 4 and 5 show time of flight curves taken at 800 V and 10 nA and 850 V and 20 nA for varying angles. Figures 6 and 7 show time of flight curves taken at 900 V and 10 nA and 950 V and 40 nA. The colors of the curves correspond to the points on the inset graph of the current distribution, giving the angular location of each of the time of flight curves. For 800 V the center of the beam has a larger average species mass than the edges of the beam. For 950 V the center of the beam has a smaller average species mass than the edges of the beam. There are no consistent trends with angle for the two intermediate voltage conditions at 850 V and 900 V. This appears to show a transition in behavior

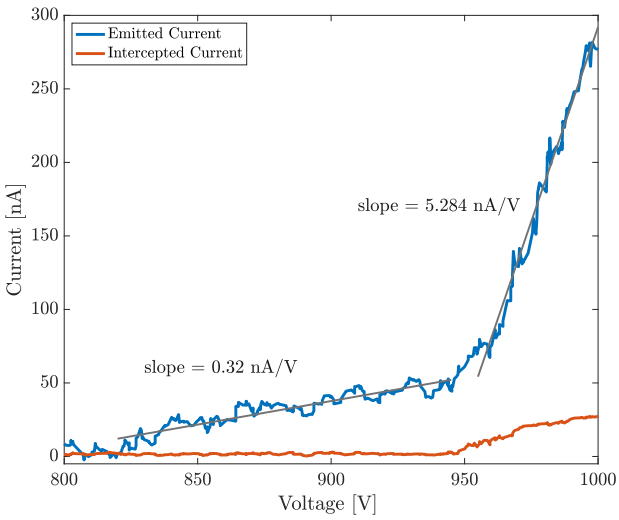

Fig. 2 Current vs. voltage curve for the single carbon emitter.

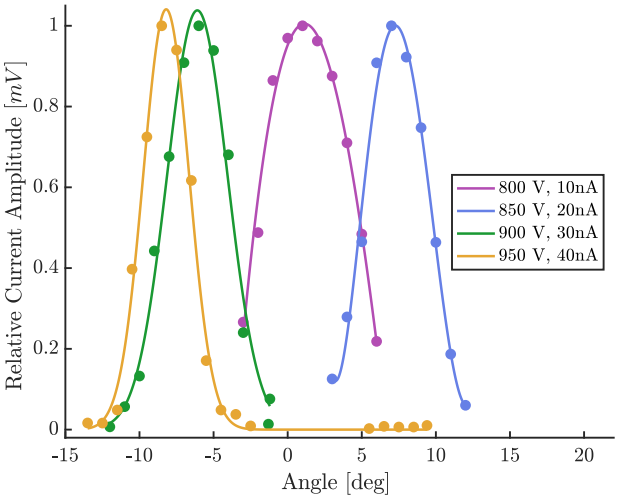

Fig. 3 Angular current distributions for the single carbon emitter at different firing voltages. The right-most 5 points for the 950 V distribution indicate the second meniscus location.

Table 1 Edge and central angles for angular current distributions.

Voltage	Center (°)	Measured Spread (°)	FWHM (°)	Amplitude (V)
800 V	1	9	7.18	0.0315
850 V	7	6	5.00	0.0692
900 V	-6	11	4.80	0.222
950 V	-8	11	3.70	0.521

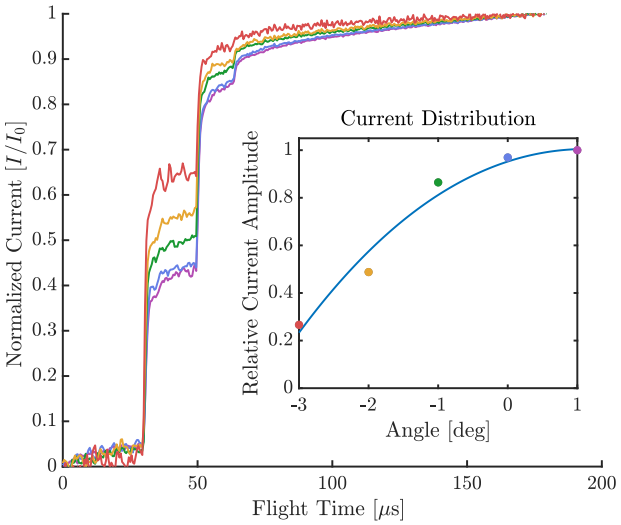

Fig. 4 Time of flight curves for 800 volts and 10 nA.

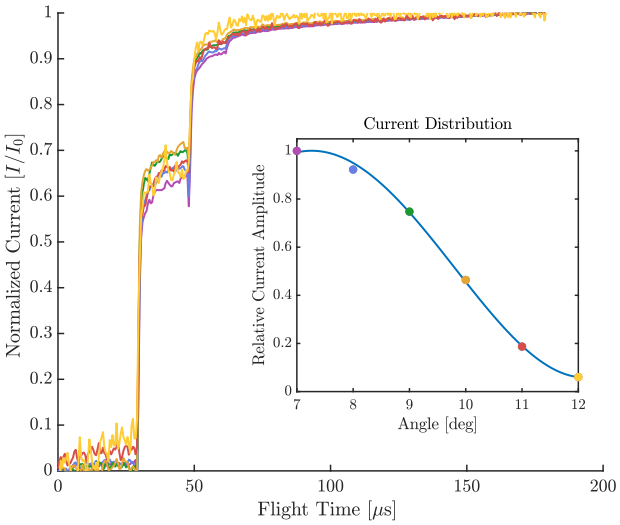

Fig. 5 Time of flight curves for 850 volts and 20 nA.

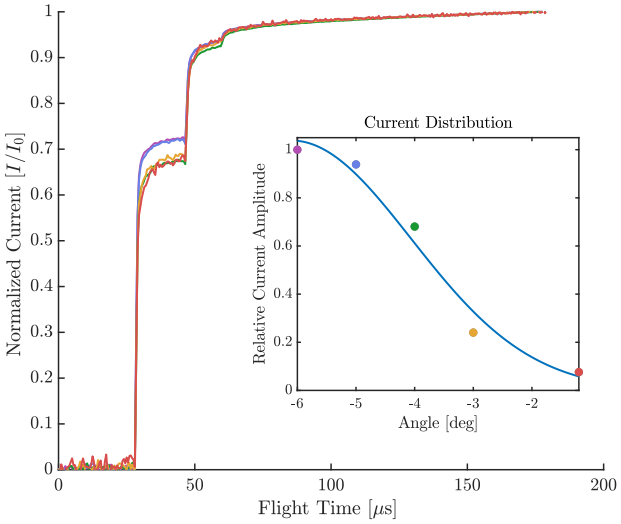

Fig. 6 Time of flight curves for 900 volts and 30 nA.

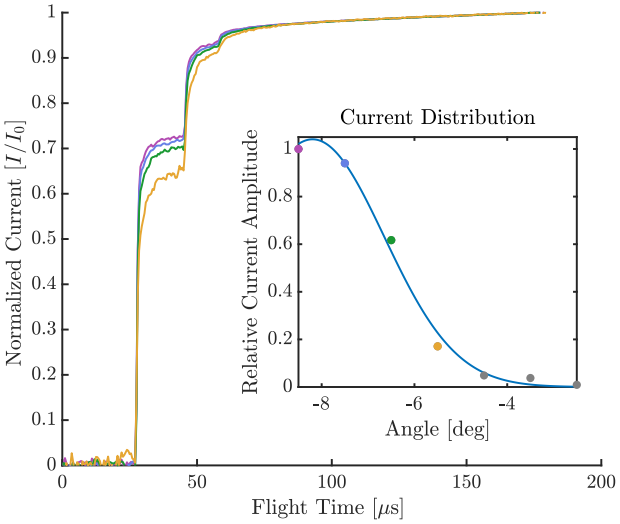

Fig. 7 Time of flight curves for 950 volts and 40 nA.

from 800 to 950 V where the average mass in the center of the beam decreases and the average mass in the edges of the beam increases.

Figure 8 compares the beam averaged time of flight curves for different voltage levels. Table 2 shows the beam fractions of different species for the highest and lowest voltage average TOF curves as determined through the post processing method developed by Jia-Richards [17]. "Heavy Species" corresponds to tetramer and larger ion clusters which are predicted to represent a negligible fraction of the beam current, though evidence for the presence of heavy ion clusters up to heptamers does exist [17]. As voltage is increased the average cluster mass decreases with more monomers and fewer dimers at the higher voltages. At the two highest voltages the difference between the average beam composition is very small. Assuming there is some error in the beam averaging process, it is difficut to determine if the highest voltage results follow the trends of the lower voltages.

B. Single Particle Trajectories

Individual cluster trajectories under varying emission conditions provide intuition for the effects of emission conditions on ion beam behavior. In particular, allowing fragmentation to occur at different timesteps during the trajectory integration can provide information about the effect of fragmentation on ion product trajectories and resulting

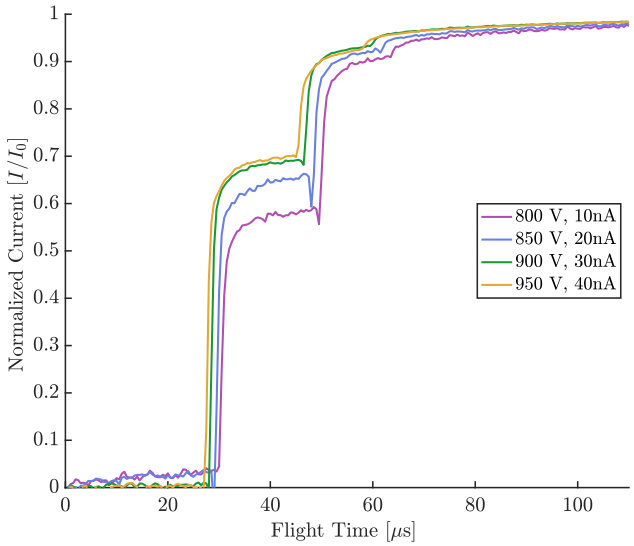

Fig. 8 Beam averaged time of flight curves for different voltage and current levels.

Table 2 Beam composition for experimental average beam time of flight curves.

Emission Conditions	Monomers	Dimers	Trimers	Heavy Species
800V and 10nA	0.532 ± 0.0129	0.344 ± 0.0227	0.076 ± 0.0226	0.046 ± 0.0134
950V and 40nA	0.635 ± 0.0105	0.256 ± 0.0191	0.0691 ± 0.018	0.0391 ± 0.0101

neutral trajectories.

The divergence angle of an ion is related to the radius of curvature of the ion trajectory, r_t, which can be obtained with an expression for the centripetal force $m_i\ a_c = q\ \mathbf{E}\cdot\mathbf{n} = m_i\frac{v_i^2}{r_t}$:

$$r_t = \frac{m_i v_i^2}{q_i\ \mathbf{E}(\mathbf{r})\cdot\mathbf{n}} = \frac{v_{i_0}^2 + 2(q_i/m_i)(\phi_0 - \phi(\mathbf{r}))}{(q_i/m_i)\mathbf{E}(\mathbf{r})\cdot\mathbf{n}} \tag{2}$$

where v_{i_0}, ϕ_0 are the initial velocity and potential energy of the ion at the at the beginning of flight on the meniscus interface. When a singly charged cluster fragments, the charge to mass ratio increases, decreasing the radius of curvature of the product ion trajectory. Steady state trajectories of ions from previous simulations indicate that ions are focused from large initial divergence angles to smaller final divergence angles during their flight from the initial location on the meniscus, through the extractor, and to the end of the electric field. Thus, fragmentation results in the charged products of fragmentation being focused towards the center of the beam. This will always be the case in pure ionic regime emission because fragmentation of dimers and trimers results in higher charge to mass ratios of the ion product. However, in droplet mode, charge to mass ratio may sometimes be reduced during ion evaporation from droplets or Coulomb explosions. This would result in spreading of the resulting ion cluster after the evaporation or Coulomb explosion event.

Figure 9 shows the final divergence angle of individually simulated dimer and trimer clusters propagated through the electric field found in the EHD simulations given varying fragmentation times. The colors correspond to the three cluster trajectories shown on the solid black line of the meniscus on the inset graph. The initial velocity condition for these clusters at the meniscus surface is given by the velocity of the fluid in the EHD simulation normal to the surface of the meniscus. When fragmentation occurs in the first few picoseconds after emission, the ion trajectory remains the same as if the product cluster were emitted directly from the meniscus. In this case $\Delta r_t \sim \frac{\Delta m_i v_i^2}{q_i \mathbf{E}\cdot\mathbf{n}}$, and for initial velocities of the ions close to 0.1 m/s [11], electrical fields close to the critical field for emission (10^9 V/m) and change of ion mass of about $\Delta m \sim 200$ amu, $\Delta r_t \sim 2\cdot 10^{-17}$ m, which is roughly 9 orders of magnitude smaller than the characteristic emission region for the ions. Similarly, when fragmentation occurs several nanoseconds after emission, after the ion has been accelerated through the majority of the potential field, and the particles have a straight trajectory

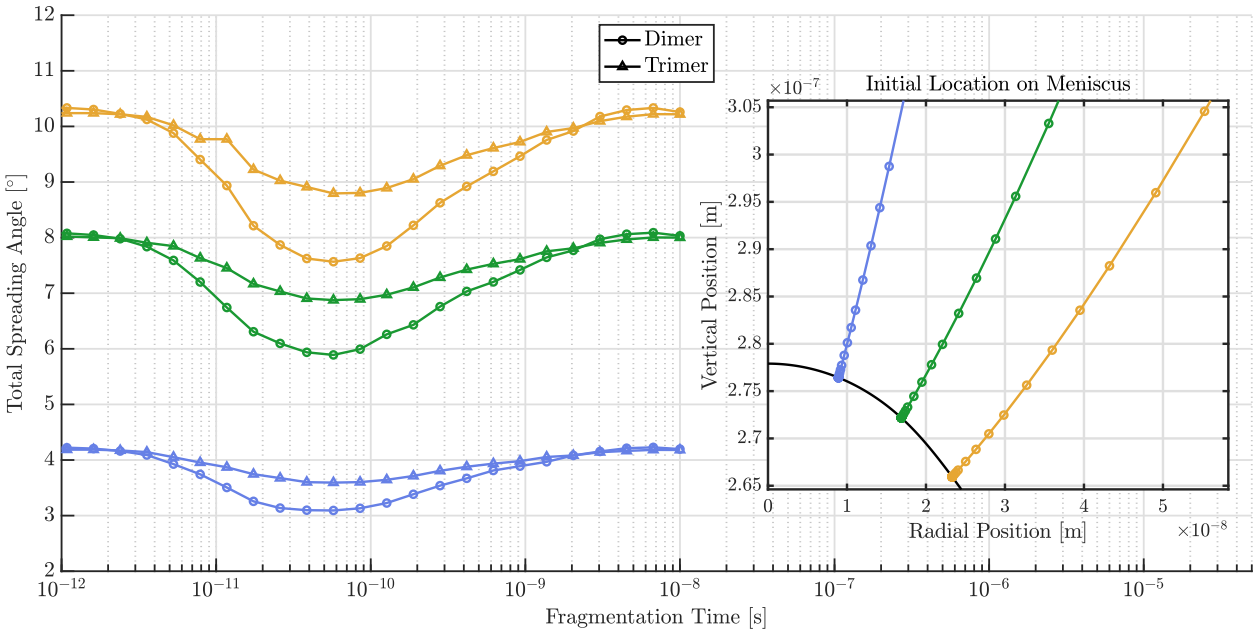

Fig. 9 Final spreading angle of ion clusters individually propagated using the electric field generated from EHD meniscus simulation. Inset graph shows the location on the equilibrated meniscus where each set of clusters are initialized and the first part of their trajectories.

where $r_t \sim \infty$, fragmentation does not change the trajectory of the ion product. However, between a few picoseconds and a few nanoseconds fragmentation results in ion products moving closer to the center axis of emission. When the ion is being focused through the aperture by the electric field, increasing the charge to mass ratio allows it to be focused in further.

For neutral byproducts of fragmentation, the divergence angle of the beam behaves differently. Neutral products of fragmentation are assumed to continue at the velocity of the parent ion cluster after fragmentation. Similar to the ion products, if fragmentation happens after the cluster has reached the end of the potential field the final divergence angle is similar to that of the unfragmented clusters. However, if fragmentation occurs earlier, between emission and hundreds of picoseconds, the divergence angle would be very similar to that of the parent ion right after being emitted from the meniscus. In this case, the meniscus profile, the structure of the meniscus emission region, and the angle at which ions are emitted is key to determine the angular span of the neutral beam, which can reach up to 47 degrees in these cases of early fragmentation. In other words, when early fragmentation occurs, the beam is not yet focused through the aperture, resulting in significantly higher spreading angles than for any of the ions in the beam. These neutrals have low energy because they fragment before the majority of the acceleration has occurred. This makes them particularly harmful to electrospray applications because they are likely to impact emitter hardware and with low energy are more likely to deposit on the hardware surface [5].

C. N-Body Beam Simulation

Full beam simulations using an N-body scheme previously demonstrated in Petro et al. [11] can be compared to experimental results to predict emission conditions. In particular, matching total ion beam spreading angle and angular beam composition can provide insight into the solvation energy and fragmentation rates of ion clusters. Figure 11 shows a comparison of the N-body simulation run at 324 nA to the experimental data for 950 V and 40 nA presented previously in this work. The total spreading angle for the simulation is more than two times larger than that of the experimental data. This is likely due to the value of the current used in the simulation. For higher currents, the contribution of the Poisson field over the Laplace field is more significant, pushing particles in the radial direction and tending to increase the divergence angle.

Inferring the value of the divergence angle is not easy: it is dependent on the initial conditions of the ions, the structure of the electric field near the emission region and the space charge present due to current evaporation. For

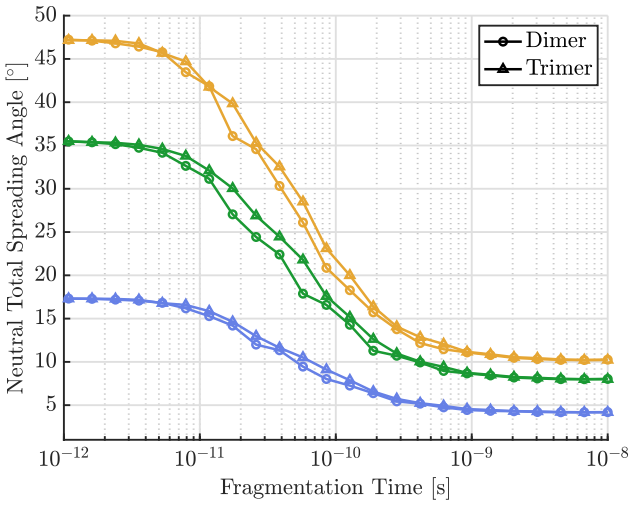

Fig. 10 Final spreading angle of neutral clusters resulting from fragmentation at varying times after emission. Colors correspond to the initial locations on the meniscus as given in Figure 9

example, competing phenomena for the deviation angle could emerge with changes in the critical field for emission. We can approximate the characteristic radius of curvature of the trajectory of the ions very roughly by approximating it as twice the radius of curvature of the emission region $r_t \sim 2r^*$. This can be seen by neglecting the initial velocity of the ions and approximating $\phi_0 - \phi(\mathbf{r}) \sim E^* r^*$, and $\mathbf{E}(\mathbf{r}) \cdot \mathbf{n} \sim E^*$ in eq. 2 where E^* is equal to the critical field of emission, and r^* to the characteristic length of emission. This approximation can be seen from the trajectory of the furthest particle from the symmetry axis in the plot on the right in figure 9, and the meniscus profile with the solid black line. From a rough balance of stresses between electric and surface tension in the emission region, we can approximate $r^* \sim \frac{4\gamma}{\epsilon_0 E^{*2}}$, and get an estimate for $r_c \sim \frac{8\gamma}{\epsilon E^{*2}}$. The higher the critical field, the smaller the radius of curvature of the trajectory will be for the particles emitted right at the end of the emission region, and the more on-axis could consequently become after travelling. However, a higher critical field would also create an elongation of the emission region to compensate for the higher electric stress, and that could involve particles being emitted with initial conditions that have higher velocity components in the radial direction. Furthermore, the reduction of the emission region size due to a higher critical field needed for emission could imply an increase of the space charge density, which could in turn enhance the radial component of the electric field and spread the beam.

Figure 12 shows a comparison of angular beam compositions between the same simulated and experimental cases. The angles have been normalized to allow comparison between the cases despite the mismatch in total spreading angle. For this simulation case the trends in the average emitted mass are opposite of those observed in the experimental results. In the experimental results average emitted mass in the center of the beam is lower than on the edges of the beam. For the simulation average emitted mass in the center of the beam is higher than on the edges of the beam. The simulation results agree with the single particle trajectory results presented previously. Namely, fragmentation will allow dimers to be focused towards the center of the beam, leaving a higher proportion of monomers on the edges. The opposite trend in the experimental results suggests that multiple emission conditions affect this angular distribution. In particular, emission of different species is currently not dependent on the meniscus location at which the cluster is initialized in the N-body simulation. If species emission probability was location dependent, this could explain why the experimental results show more dimers on the edges of the beam despite fragmentation causing them to be focused towards the center.

The combination of these emission conditions results in the full angular current distributions and beam composition. Thus, accurately reproducing these behaviors is key to understanding all of the emission conditions.

IV. Conclusions

In summary, this work presents experimental characterization of a single electrospray emitter operating in the pure ionic regime. Angular properties were investigated with angular current distributions and angular time of flight mass spectrometry. Angular current measurments indicate that the central axis of emission is dependent on firing voltage and

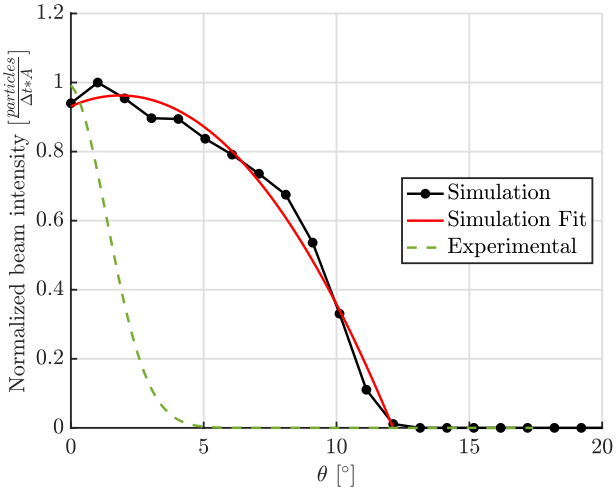

Fig. 11 Comparison of simulated and experimental angular current distributions. Simulation is for 324 nA and experimental data is for 950 V and 40 nA.

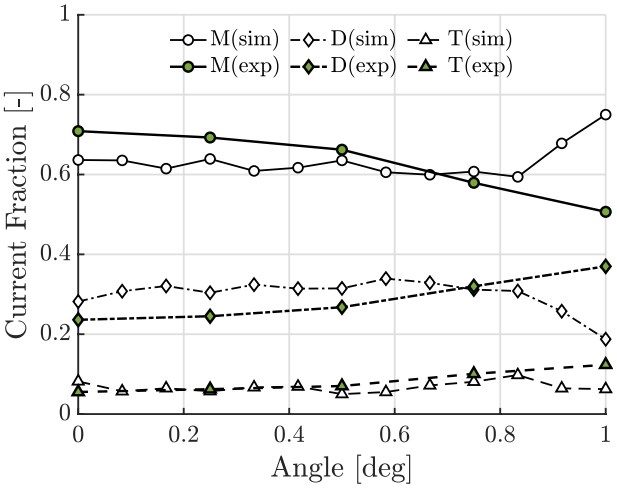

Fig. 12 Comparison of simulated and experimental angular beam composition. Simulation is for 324 nA and experimental data is for 950 V and 40 nA.

varies up to 10°. Angular beam composition also varies with firing voltage. As firing voltage increases the highest average emitted mass moves from the center of the beam to the edges.

Single particle trajectories were found from electrohydrodynamic simulations of meniscus shape and current density on the surface of the meniscus. These indicate that while fragmentation focuses the resulting ions up to 3° closer to the central axis of the beam, neutral products of fragmentation spread up to 47° away from the center of the beam, potentially impacting thruster hardware and decreasing lifetime.

Full beam simulations were compared to experimental results. Simulated angular spread was significantly higher than that found in experiments. Additionally, angular variation of beam composition did not match. Future work will focus on determining the emission conditions to match the simulation and experimental results including the critical electric field for emission, fragmentation rates, and the dependence of species emission on initial meniscus location.

References

[1] Coles, T., Fedkiw, T., and Lozano, P., "Investigating Ion Fragmentation in Electrospray Thruster Beams," *48th AIAA/ASME/SAE/ASEE Joint Propulsion Conference & Exhibit*, American Institute of Aeronautics and Astronautics, Atlanta, Georgia, 2012. https://doi.org/10.2514/6.2012-3793, URL http://arc.aiaa.org/doi/abs/10.2514/6.2012-3793.

[2] Fedkiw, T. P., and Lozano, P. C., "Development and characterization of an iodine field emission ion source for focused ion beam applications," *Journal of Vacuum Science & Technology B: Microelectronics and Nanometer Structures*, Vol. 27, No. 6, 2009, p. 2648. https://doi.org/10.1116/1.3253604, URL http://scitation.aip.org/content/avs/journal/jvstb/27/6/10.1116/1.3253604.

[3] Lozano, P., and Martinez-Sanchez, M., "Efficiency Estimation of EMI-BF4 Ionic Liquid Electrospray Thrusters," *41st AIAA/ASME/SAE/ASEE Joint Propulsion Conference & Exhibit*, American Institute of Aeronautics and Astronautics, Tucson, Arizona, 2005. https://doi.org/10.2514/6.2005-4388, URL http://arc.aiaa.org/doi/abs/10.2514/6.2005-4388.

[4] Krejci, D., Mier-Hicks, F., Fucetola, C., Lozano, P., Schouten, A. H., and Martel, F., "Design and Characterization of a Scalable ion Electrospray Propulsion System.pdf," *Joint Conference of 30th International Symposium on Space Technology and Science, 34th International Electric Propulsion Conference and 6th Nano-satellite Symposium*, Hyogo-Kobe, Japan, 2015.

[5] Cidoncha, X. G., Lozano, P. C., Bendimerad, R., Petro, E. M., and Hampl, S. K., "Modeling and Characterization of Electrospray Propellant-Surface Interactions," *2022 IEEE Aerospace Conference (AERO)*, IEEE, Big Sky, MT, USA, 2022, pp. 1–11. https://doi.org/10.1109/AERO53065.2022.9843583, URL https://ieeexplore.ieee.org/document/9843583/.

[6] Coles, T. M., and Lozano, P. C., "Investigating Efficiency Losses from Solvated Ion Fragmentation in Electrospray Thruster Beams," *49th AIAA/ASME/SAE/ASEE Joint Propulsion Conference*, American Institute of Aeronautics and Astronautics, San Jose, CA, 2013. https://doi.org/10.2514/6.2013-4033, URL https://arc.aiaa.org/doi/10.2514/6.2013-4033.

[7] Miller, C. E., "Characterization of Ion Cluster Fragmentation in Ionic Liquid Ion Sources," Ph.D. thesis, Massachusetts Institute of Technology, 2019.

[8] Miller, C. E., and Lozano, P. C., "Measurement of the dissociation rates of ion clusters in ionic liquid ion sources," *Applied Physics Letters*, Vol. 116, No. 25, 2020, p. 254101. https://doi.org/10.1063/5.0006529, URL http://aip.scitation.org/doi/10.1063/5.0006529.

[9] Schroeder, M., "Numerical Characterization of Fragmentation in Ionic Liquid Clusters," Master's thesis, Massachusetts Institute of Technology, May 2021.

[10] Petro, E., Miller, C. E., Schmidt, J., and Lozano, P. C., "Development of an Electrospray Fragmentation Model for Kinetic Plume Modeling," *36th International Electric Propulsion Conference*, Vienna, Austria, 2019.

[11] Petro, E. M., Gallud, X., Hampl, S. K., Schroeder, M., Geiger, C., and Lozano, P. C., "Multiscale modeling of electrospray ion emission," *Journal of Applied Physics*, Vol. 131, No. 19, 2022, p. 193301. https://doi.org/10.1063/5.0065615, URL https://aip.scitation.org/doi/10.1063/5.0065615.

[12] Krejci, D., Mier-Hicks, F., Thomas, R., Haag, T., and Lozano, P., "Emission Characteristics of Passively Fed Electrospray Microthrusters with Propellant Reservoirs," *Journal of Spacecraft and Rockets*, Vol. 54, No. 2, 2017, pp. 447–458. https://doi.org/10.2514/1.A33531, URL https://arc.aiaa.org/doi/10.2514/1.A33531.

[13] Petro, E., Bruno, A., Lozano, P., Perna, L. E., and Freeman, D., "Characterization of the TILE Electrospray Emitters," *AIAA Propulsion and Energy 2020 Forum*, American Institute of Aeronautics and Astronautics, 2020. https://doi.org/10.2514/6.2020-3612, URL https://arc.aiaa.org/doi/10.2514/6.2020-3612.

[14] Perez-Martinez, C. S., and Lozano, P. C., "Ion field-evaporation from ionic liquids infusing carbon xerogel microtips," *Applied Physics Letters*, Vol. 107, No. 4, 2015, p. 043501. https://doi.org/10.1063/1.4927481, URL http://aip.scitation.org/doi/10.1063/1.4927481.

[15] Courtney, D. G., Dandavino, S., and Shea, H., "Comparing Direct and Indirect Thrust Measurements from Passively Fed and Highly Ionic Electrospray Thrusters," *Journal of Propulsion and Power*, 2015, p. 23.

[16] Perez-Martinez, C., Guilet, S., Gogneau, N., Jegou, P., Gierak, J., and Lozano, P., "Development of ion sources from ionic liquids for microfabrication," *Journal of Vacuum Science & Technology B, Nanotechnology and Microelectronics: Materials, Processing, Measurement, and Phenomena*, Vol. 28, No. 3, 2010, pp. L25–L27. https://doi.org/10.1116/1.3432125, URL http://avs.scitation.org/doi/10.1116/1.3432125.

[17] Jia-Richards, O., "Quantification of ionic-liquid ion source beam composition from time-of-flight data," *Journal of Applied Physics*, Vol. 132, No. 7, 2022, p. 074501. https://doi.org/10.1063/5.0094699, URL https://aip.scitation.org/doi/10.1063/5.0094699.

[18] Coffman, C. S., Martínez-Sánchez, M., and Lozano, P. C., "Electrohydrodynamics of an ionic liquid meniscus during evaporation of ions in a regime of high electric field," *Physical Review E*, Vol. 99, No. 6, 2019, p. 063108. https://doi.org/10.1103/PhysRevE.99.063108, URL https://link.aps.org/doi/10.1103/PhysRevE.99.063108.

[19] Gallud Cidoncha, X., "A comprehensive numerical procedure for solving the Taylor-Melcher leaky dielectric model with charge evaporation.pdf," Master's thesis, Massachusetts Institute of Technology, 2019.

[20] Gallud, X., and Lozano, P. C., "The emission properties, structure and stability of ionic liquid menisci undergoing electrically-assisted ion evaporation," *Journal of Fluid Mechanics*, Vol. 933, 2021. URL http://arxiv.org/abs/2109.12274, arXiv: 2109.12274.

[21] Barnes, J., and Hut, P., "A hierarchical O(N log N) force-calculation algorithm," *Nature*, Vol. 324, No. 6096, 1986, pp. 446–449. https://doi.org/10.1038/324446a0, URL http://www.nature.com/articles/324446a0.

[22] Hampl, S. K., Waggoner, M., Petro, E. M., Gallud, X., and Lozano, P. C., "Comparison of Computational Methods for Modeling an Electrospray Plume with a n-body Simulation.pdf," Boston, Massachusetts, USA, 2022.